Available online at www.sciencedirect.com

jmr&t Journal of Materials Research and Technology

journal homepage: www.elsevier.com/locate/jmrt

Direct additive manufacturing as spring of new tool steels

Francisco R. Cruz [a,*], *Nanci Alves* [b], *Teresa Vieira* [a]

[a] *CEMMPRE, Department of Mechanical Engineering, University of Coimbra, R. Luís Reis Santos, Coimbra 3030-788, Portugal*

[b] *ITJ – Internacional Moldes, Lda., Embra, Marinha Grande, 2430-528, Portugal*

ARTICLE INFO

Article history:
Received 30 June 2023
Accepted 17 August 2023
Available online 22 August 2023

Keywords:
Additive manufacturing
Powder bed fusion
Precipitation hardening
Vanadium carbide
Nanoprecipitates
Steel matrix nanocomposites

ABSTRACT

Additive manufacturing (AM) is now common in production of metallic matrixes with/without reinforcements (nanoprecipitates) to improve functional and structural mechanical properties of 3D objects. The presence of liquid phase in direct processes allows the possibility to change the conventional chemical composition of materials homogeneously. Powder Bed Fusion (PBF), in which the high nonequilibrium solidification nature resembles a localized high cooling rate but allowing, still the formation nanocarbides in-situ. Thus, it will be the suitable technology to tailor novel functionally gradient metallic materials. Nevertheless, this character is only present in the upper layers due to the shaping being made layer by layer. During shaping, the previous layers undergo post heat treatments contributing for growing the carbide dimension. Hence, metallic alloys can be developed simultaneously with the processing stage by changing the chemical composition by addition of fundamental elements to the matrix powder. In tool steel the improvement of hardening carbide content can contribute to a better performance concerning hardness and abrasion wear resistance. The present study concerns the addition of vanadium powder and allotropes of carbon, in correlation with the partition coefficient between vanadium and carbon in the steel selected - AISI H13, processed by selective laser melting (PBF/SLM), without requiring adjusting the processing parameters. The hardness attained is analogous to high speed steels, since this allows layers with a similar matrix to the wrought tool steel but with higher content of hardening carbide (VxCy). The sustainability of the final product is evident.

1. Introduction

Additive manufacturing (AM) of metallic powder is becoming more and more significant for processing metallic 3D objects. The selection of AM versus replicative or subtractive processes is up to now mainly due to the new design potentials, which are either impossible or very costly with typical approaches [1]. The AM must build products that are much more efficient, less dependent on the cost and availability of raw materials [2], and be able to quickly readapt to new imposed boundary conditions. In the molds industry for injection molding of polymers or other feedstocks enriched in inorganic powder particles (metallic and ceramic), the potential of AM is

* Corresponding author.
E-mail address: franciscorrcruz@gmail.com (F.R. Cruz).

https://doi.org/10.1016/j.jmrt.2023.08.176

evident to optimize new geometries, e.g., cooling channels in inserts based on conformal [3–5] and recently in other new cooling inside systems, as the denominated constructal cooling [6,7]. These systems, as the direct process denominated Powder Bed Fusion, in particular Selective Laser Melting (PBF/SLM), allows the improvement of the gloss of injected 3D objects. In PBF/SLM, different parameters must be take into account, mainly are associated with the volumetric energy density (VED) [8]. Nevertheless, the gloss of the 3D object is also the result of the inserts hardness and the surface protection, which is common to be attained by the presence of a hard coating [9]. However, two main problems can occur, such as lacking adhesion to the substrate and a significant increase in the mold cavity/insert cost [10].

The main challenges for AM [11] are developing materials with outstanding properties that will enable significantly more efficient/sustainable processes and diminishing the dependency on critical raw materials by contributing to more flexibility in materials composition. The materials commonly selected to produce molding inserts for injection molding are mainly chosen by hardness, abrasion wear resistance, high thermal fatigue [12], and for some feedstocks by corrosion resistance [13]. The most applied tool steels [14] are based on C–Cr–Mo–Si–V, like H13(AISI) for molding parts made from conventional tool steels. They can achieve suitable properties for the envisaged application, injection molding, when heat-treated. The wrought AISI H13 after quenching, has a microstructure mainly composed of martensite (α") [8]. Besides this metastable phase, some authors [15] had detected a significant amount of residual austenite (γ) up to 30% when H13 powder is manufactured by PBF/SLM. Carbides based on chromium and vanadium are evident in 3D objects without post heat treatment. In PBF/SLM, the geometry is generated by melting powder layer by layer with a high-energy laser beam and then rapidly solidified. Due to the tensile stress developed by the high cooling rate attained in the PBF/SLM, the increase of residual austenite is attended. However, the deposition layer by layer contributes to a continuous tempering of the quenched layers. These successive heat treatments can decrease the residual austenite into tempered martensite and promote the precipitation of hardening nanocarbides. The effect of the building process layer by layer and selected parameters [16] may contribute to the tempering of previous deposited layers constituted by martensite and retained austenite in tempered martensite (α') with secondary carbides [17–19]. However, some authors claim that no formation of precipitates occurred during the PBF/SLM process [15,20–22]. Besides the non-negligible partition coefficient of vanadium (vanadium carbide: vanadium matrix), the vanadium content of AISI H13 is $\leq$1 wt % and the minimum content of vanadium to form carbides, associated with the cooling rate of PBF/SLM, can contribute directly to a microstructure composed by martensite (lathes) with or without residual austenite, where after quenching the main alloy elements (Cr, Mo, V) are in solid solution of Fe structure. The successive deposited layers can also promote the decrease of the residual austenite and increase of secondary precipitation of coherent carbides, associated with a significant increase of the steel hardness [15]. Nevertheless, it must be assured that the temperature/time of all layers deposited to obtain the 3D object selected does not overcome the limits of tempering temperature/time suitable to ensure that hardness attained will be higher than the heat-treated AISI H13 wrought steel after multi-tempering (2 h, 500 °C).

Table 1 – Chemical composition of the steel mixtures (in wt. %).

Steel	C	Cr	Mo	V
H13	0.4	5	1.5	1.0
H13+V	0.4	4.7	1.4	5.6
H13+V+G	1.2	4.7	1.4	5.6

The goal of the present study is to evaluate the role of vanadium addition in AISI H13 during the processing by PBF/SLM. A new route to build 3D objects from AISI H13 powder, but with a new chemical composition of a high alloy steel, having a superior mechanical property than AISI H13, whatever the making process: fusion, reduction, electro-deposition or powder technology. Nevertheless, it must be demonstrated the presence or not of nanocarbides after PBF/SLM cooling, particularly in the surface layers, which are not submitted to the tempering effects. The target is to reach the highest hardness on the 3D object surface without post-treatments, by increasing the density of dislocations and coherent precipitation. The research available in the published papers are restricted and concerning mainly on the addition of carbides based on titanium and tungsten to steel matrices, and not on self-created nanocarbides during the additive manufacturing.

2. Materials and methods

2.1. Feedstock

In this study, three powder mixtures were applied to the 3D built process by PBF/SLM (Table 1): AISI H13; AISI H13 with vanadium powder; and AISI H13 with vanadium and graphene powder particles. Gas atomized AISI H13 powder was provided by Oerlikon Metco, NY, USA; the vanadium powder by Nanografi, Turkey; and graphene by Graphene Supermarket, Calverton, NY, USA.

For all powder particles selected, the particle size and particle size distribution were measured by a laser particle size analyzer from Malvern Mastersizer 2000, Malvern Instruments Ltd, Worcestershire, UK. Powder morphology/topography and microstructures of 3D objects after additive manufacturing were evaluated using optical microscopy (OM) Leica DM4000 M LED connected with a LEICA MC190 HD camera (Ernst Leitz GmbH, Wetzlar, Germany) and a scanning

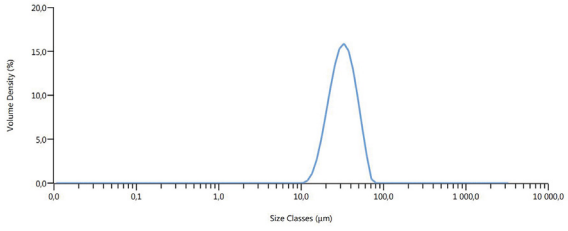

Fig. 1 – AISI H13 powder particle size distribution.

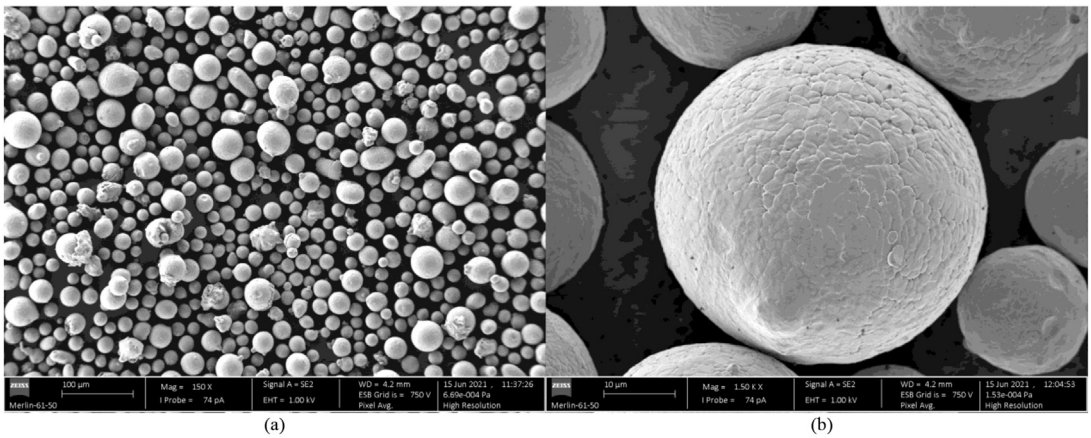

Fig. 2 – Micrographies (SEM) of AISI H13 particles showing powder particle size and particle size distribution (a); particle shape and topography (b).

electron microscope (SEM) FEI Quanta 400FEG (FEI Europe BV, Eindhoven, Netherlands) equipped with energy-dispersive spectroscope (EDAX Genesis X4M, EDAX Smart Insight, Mahwah, New Jersey, USA). X-ray diffraction (XRD) was applied for phase identification before and after PBF/SLM. A Philips X'Pert, Philips, Eindhoven, Netherlands, (Bragg-with Brentano geometry (θ-2θ), cobalt radiation (λkα1 = 0.1789 nm and λkα2 = 0.1793 nm).

2.1.1. *AISI H13 powder*

The chemical composition of AISI H13 is summarized in Table 1. The particle size values were D_{10} = 19.7 μm, D_{50} = 32.0 μm, D_{90} = 50.2 μm (Fig. 1).

Whatever the particle size the particle shape has a shape factor close to 1 (Fig. 2a and b). Moreover, they do not present any satellites that could have a significant role in decreasing the powder flowability, which is significant for PBF/SLM processability (Fig. 2a). Nevertheless, evidence of agglomeration/aggregation can be perceptible in Fig. 2b.

The XRD reveals the presence of two phases: ferrite/martensite and austenite (Fig. 3). The carbides present in annealed AISI H13 bulk: $M_{23}C_6$ (M = Cr, Mo, V…) and the possible V_xC_y were not detected in both cases by XRD, due to their dimension and content.

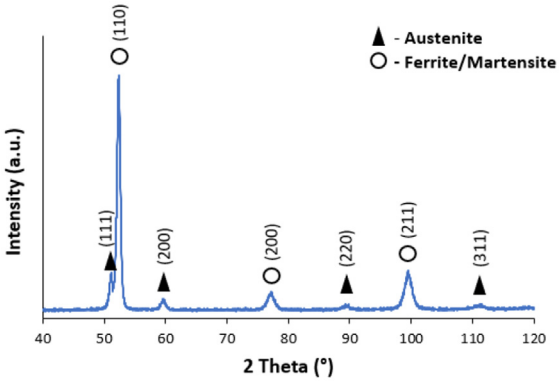

Fig. 3 – AISI H13 powder X-ray diffractogram.

2.1.2. *Vanadium powder*

The vanadium powder had particle sizes of D10 = 6.86 μm, D50 = 21.5 μm, D90 = 44.0 μm (Fig. 4), a shape factor smaller than 1 (Fig. 5a), and the surface with high roughness (Fig. 5b and c), and no contamination (Fig. 6). However, milling the different powder particles was essential to decrease this abnormal surface morphology, and the powder shape factor becomes close to 1. The percentage of V in the feedstock studied was 5 wt%. The mixture powder of 95 wt% H13 and 5 wt% V was ball-milled in an argon atmosphere for 30 min under the designed conditions of a ball-to-powder weight ratio of 5:1 and a rotation speed of 200 rpm. In the planetary ball-milling device, the milling tank and 10 mm in diameter balls were made of martensitic stainless steel with high abrasion resistance to avoid element contamination in the powder mixture.

The milling process was intended to homogenize the mixture of AISI H13 and vanadium powder particles. The spherical shape of the H13 powders (Fig. 2b) was preserved due to the short milling period and relatively low rotation speed. Since the uniformity of the mixed powder will affect the microstructure of the 3D object after processing, the feedstock should be as homogeneously distributed as possible (Fig. 7a and b).

2.1.3. *Allotrope of carbon*

For the third mixture, graphene (Graphene Supermarket, Calverton, NY, USA) was added to the H13+5V wt.% according to the atomic ratio C:V in V_4C_3, primary carbide typical of tool steels, no total dissolved during quenching heat treatment.

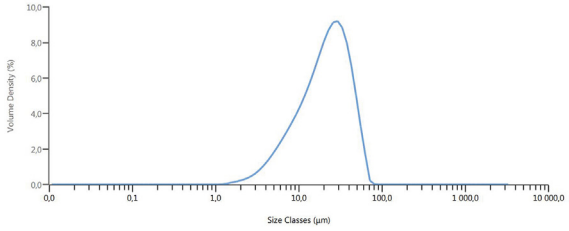

Fig. 4 – Vanadium powder particle size distribution.

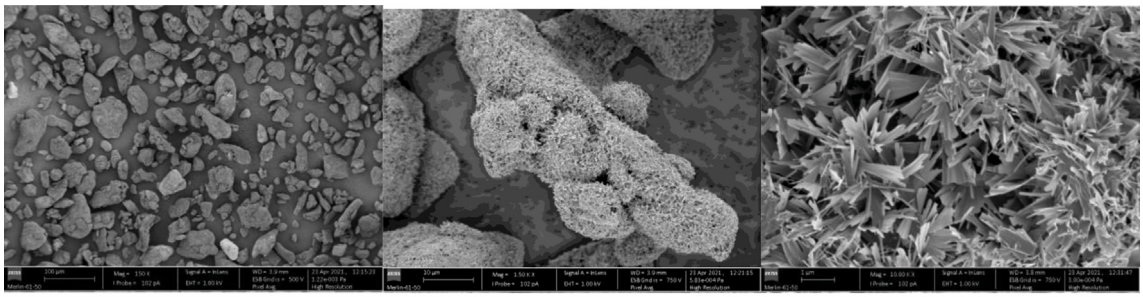

Fig. 5 – Micrographies (SEM) of vanadium powder exhibiting: powder particle size and particle size distribution (a); particle shape and topography (b); powder surface before milling (c).

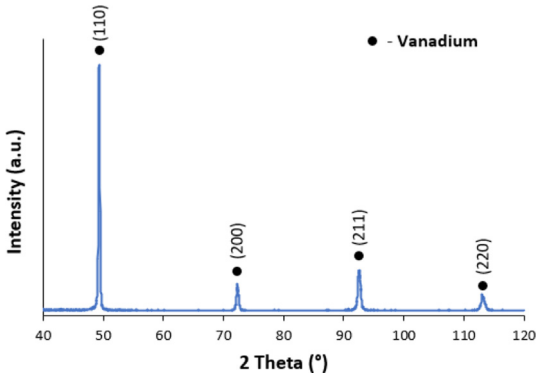

Fig. 6 – Vanadium powder X-ray diffractogram (right).

The graphene flakes (Fig. 8) had 98.5% purity, with a specific surface area lower than 15 m^2/g, an average flake thickness of 60 nm, and particle (lateral) size between 3 and 7 μm.

After undergoing the same mixing conditions detailed in 2.1.2., the H13+V+G feedstock displayed uniform dispersion of AISI H13, vanadium and graphene particles (Fig. 9). The analysis parameters were configured to identify characteristic X-rays emitted by iron, chromium, molybdenum, vanadium, and carbon elements. Notably, carbon, being a low atomic number element, exhibited reduced detection accuracy during EDS, and therefore required higher magnification.

2.2. *PBF/SLM manufacturing and characterization*

The 3D object of H13 (AISI) was carried out by standard PBF/SLM equipment (TruPrint1000, Trumpf, Germany) from powder particles. A continuous mode ytterbium fiber laser with 250 W maximum power and estimated beam diameter at the focal point of 75 μm was selected. The building chamber was under an argon atmosphere that was continually injected during processing to strictly preserve the oxygen content below 50 ppm. Processing parameters were maintained throughout the 3D object-built height, and they are, as follows: laser power (P) was set at 120 W; the strategy was a two-contour with 45° infill scanning, with a 90° increase per layer; a laser hatch distance (h) of 90 μm and each powder layer was scanned once by the laser, with a layer thickness (d) of 30 μm. The laser scan speed (v) was 700 mm/s (Table 2). Thus, the volumetric energy density VED [8] of 64 J/s [23] was calculated by equation (1):

$$VED = \frac{P}{hdv} \quad (1)$$

The selected conditions (Table 2) let to obtain 3D objects of high quality (Fig. 10). The cylinder ($\varphi = 10$ mm; h = 5 mm) built by PBF/SLM was scanned by microCT (X-ray micro-computed tomography) using a Bruker SkyScan 1275 (Bruker, Kontich, Belgium) to detect inside defects, particularly porosity higher than 10 μm. An acceleration voltage of 100 kV and a beam current of 100 μA was set while using a 1 mm copper filter and

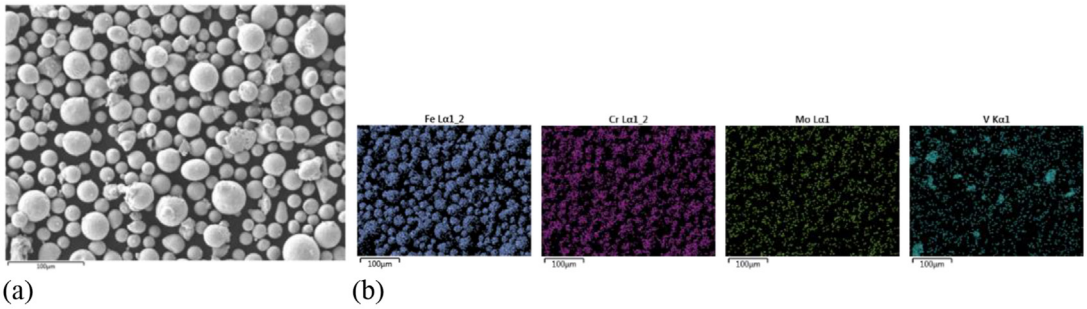

Fig. 7 – SEM image of AISI H13+V (a) and EDS mapping of Fe, Cr, Mo and V in the mixture (b).

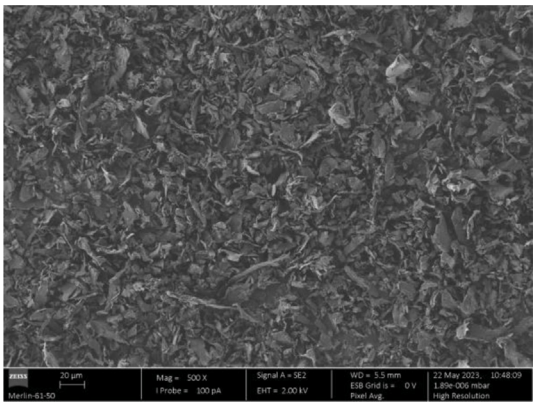

Fig. 8 – Micrography of graphene flakes.

step-and-shoot mode. The pixel size was set to 7 μm, and random mode was used. 901 projection images were acquired at 0.4° angular step with 10 frames average per step using an exposure time of 245 ms. The microCT images were reconstructed with dedicated manufacturer software.

The existing phases after PBF/SLM were analyzed by XRD diffraction. The microstructures were observed under optical microscopy (OM) and scanning electron microscope (SEM). The relative content of phases was measured by ImageJ software. Phase identification was also performed with the assistance of transmission electron microscopy (TEM). Thin sections at the top surface of the AISI H13 cylinders with or without vanadium and vanadium +carbon additions were obtained using FIB ex-situ lift-out technique, by a Ga^+ gun from FEI Helios Nanolab 600 Dual Beam (USA) at 30 kV for Pt deposition and rough milling. The thin section was removed with a micromanipulator and placed onto an Omniprobe copper grid to be subsequently thinned down for electron transparency, with decreasing ion currents, to a thickness below 50 nm. The thin foils were then imaged with a JEOL 2010F FEG-TEM (JEOL USA, Inc., Massachusetts, USA) operating at 200 kV, carrying out high-resolution transmission electron microscopy (HRTEM) and selected area electron diffraction (SAED).

After finishing with SiC papers and diamond polishing pads (Struers S.A.S, Hovedstaden, Denmark), microhardness measurements were performed with a Shimadzu HMV microhardness tester (Shimadzu Corp., Kyoto, Japan), according to ISO 6507–2:2018. For each measurement, a load of 5 N was applied for 15 s with a dwell time of 15 s by a Vickers indenter. The average Vickers hardness measurements were obtained through five indentations on the polished surfaces of the specimens, distant from the indentation marks. Nanoindentation of the specimens was taken to a computer-controlled nanoindenter (NanoTest, Micro Materials Limited, Wrexham, UK) equipped with a Berkovich triangular pyramidal diamond indenter. The transferal to the indenter was carried out using a computer-controlled X–Y table and was performed in load control mode, by selecting an area through an optical microscope. For each specimen, it was performed a programmed matrix of 4 rows × 10 columns (total of 40 indentations), with an indentation maximum load of 1.5 mN. Both distances between rows and columns were 5 μm. Loading/unloading was carried out in 5 s, with 2 s at maximum load. Hardness (H) and reduced Young modulus (Er) were calculated using the Oliver and Pharr analysis method [24].

Table 2 – Processing parameters applied in the manufacturing of AISI H13 based feedstocks.

Laser power - P (W)	120
Scan speed - v (mm/s)	700
Layer thickness - d (μm)	30
Hatch distance - h (μm)	90
Atmosphere	Argon
Pre-heating (°C)	–

3. Results and discussion

The AISI H13 tool steel has three main alloy elements which aim to improve corrosion resistance, such as chromium, and to increase the softening resistance for temperatures up to 550 °C as Mo and V elements. At equilibrium conditions (annealed) the main metallic elements are in solid solution in the ferrite and as carbides, depending on the affinity of the alloy element to carbon (V > Mo > Cr) and content in the nominal chemical composition of the steel (Cr > 4–5; Mo > 2–3 and V ≥ 1 wt%). The partition coefficient is defined as the alloy element ratio in iron-based matrix solid solution and its carbide (Cr = 3:2; Mo = 2.5:2.5; V = 1:4). Thus, wrought H13 tool steel as annealed is constituted by ferrite, $Cr_{23}C_6$, and V_4C_3. After heating to temperatures 1020–1050 °C for 30 min followed by quenching (high cooling rate but not enough to stabilize austenite), the phases are martensite+austenite and V_4C_3 (HV10 = 550–600); and after tempering at 500-550 °C the

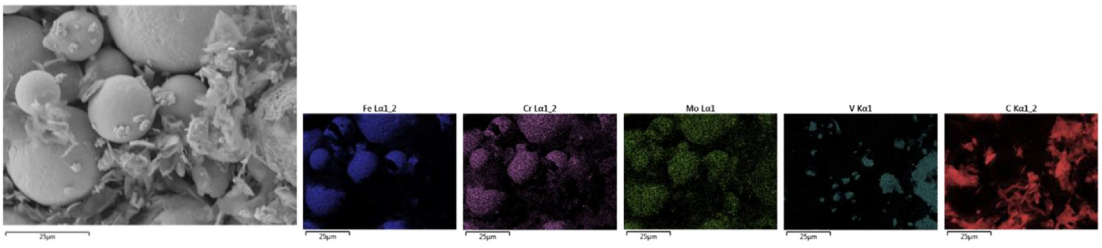

Fig. 9 – SEM image of H13+V+G mixture and respective EDS mapping of Fe, Cr, Mo, V, and C.

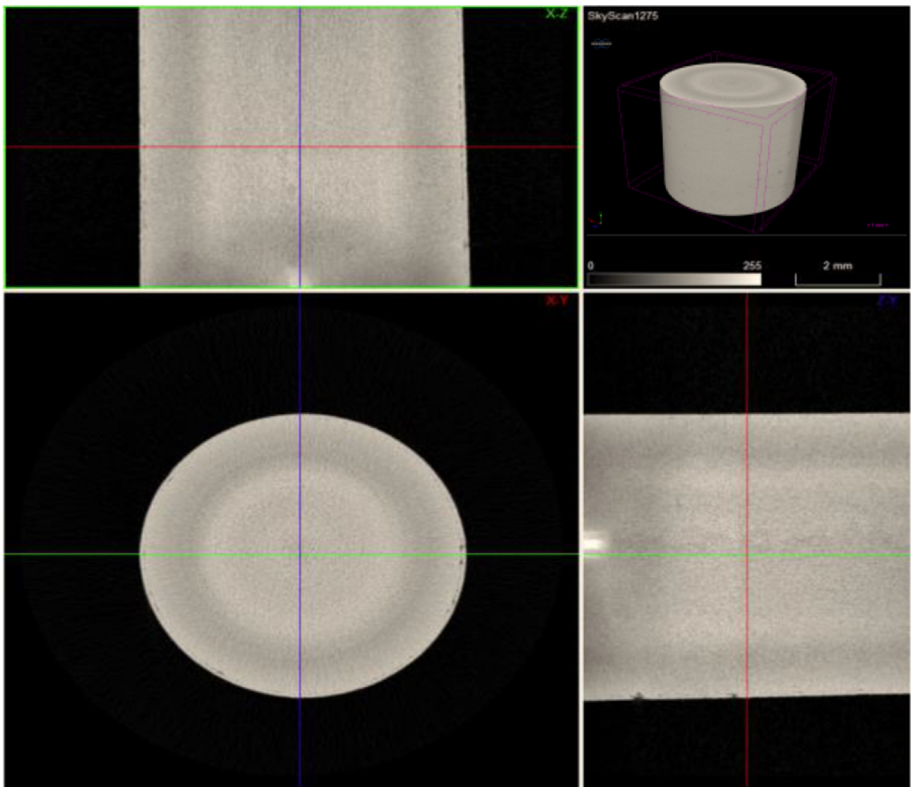

Fig. 10 – MicroCT (4x) of the H13+5V+0.8 C wt.% after PBF/SLM processing.

phases are tempered martensite (α′) and fine carbides (V_4C_3) [25]. However, V–C has many different stoichiometries: V_2C, V_4C_3, V_5C_3, V_6C_5, V_8C_7, and VC (C/V from 0,5 to 1) [20]. In alloy steels with vanadium in their phase composition, VC and V_4C_3 are typical [26]. However, new technologies of processing, like PBF/SLM, can contribute to other stoichiometries, which are mechanical, dynamical, and thermodynamically stable. Thus, with new properties as reinforcement, in particular, the hardness can be improved. This is the case of V_5C_3, which is abnormally much harder than neighboring compounds in the V–C phase diagram [27].

In order to study the influence of PBF/SLM on the microstructure, the top subsurface of the as-builds cylinders from H13 feedstock manufactured by PBF/SLM, referenced by original quench material, were examined using OM, SEM, and TEM microscopies. For OM observation, specimens were polished and chemically etched using 2 ml acid nitric in 100 ml ethanol, at room temperature. The images from 20 μm of the cylinder surface show cellular dendrites with different orientations (Fig. 11, left). This is also confirmed by SEM (Fig. 11, right). The cellular structure on the sectioned surface presents different morphology corresponding to different grain orientations, either cellular or columnar depending on the direction of observation. The unique microstructure formation within the PBF/SLM processing is attributed to various factors, commonly associated with residual stress resulting from the extremely high cooling rates. According to Ge Wang et al. [28], the local inherent non-uniformity in laser scanning heating

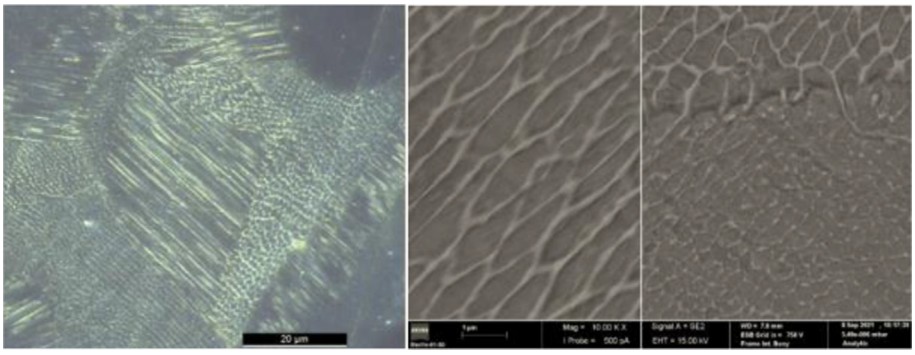

Fig. 11 – Optical microscopic image (OM) of H13 as-built, in the XY plane (400x) (left), and a detail (SEM) (right).

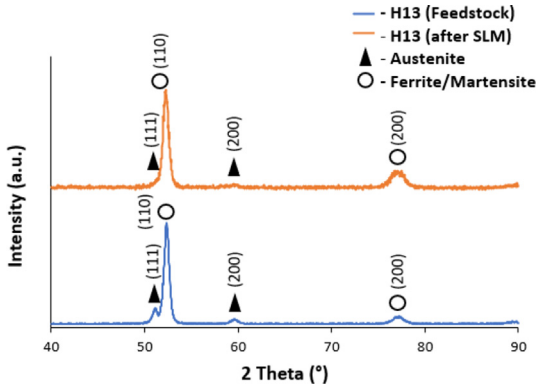

Fig. 12 – X-ray diffractograms of H13 as-built (top) and feedstock (bottom).

and cooling contributes to the increase of residual stress, due to the adaptation to local expansion or contraction mismatch. If the magnitude of residual stress reaches a critical level leading to plastic deformation, dislocation accumulates and undergoes self-assembly, forming a cellular pattern.

The size of the cellular structure was about 1 μm (Fig. 11, right) due to the high cooling rate (typically about 10^5 K/s) in the PBF/SLM process.

In the microstructure can be detected the matrix (grey) constituted by ferrite/martensite, and the cellular boundary (white) is ascribed by some authors as retained austenite, which could be present due to the high cooling rate of layers as in the atomization of powder particles. Nevertheless, the XRD diffractogram (orange) shows vestiges of diffraction peaks that can be indexed as planes of retained austenite phase (Fig. 12).

The low percentage of vanadium (≈1%) also contributes to a very small fraction of vanadium carbides, not discernible in the X-ray diffractograms. The size of the carbides and the resolution of the optical microscope made difficult the observation of these hard carbides after cooling. In SEM (EBSD

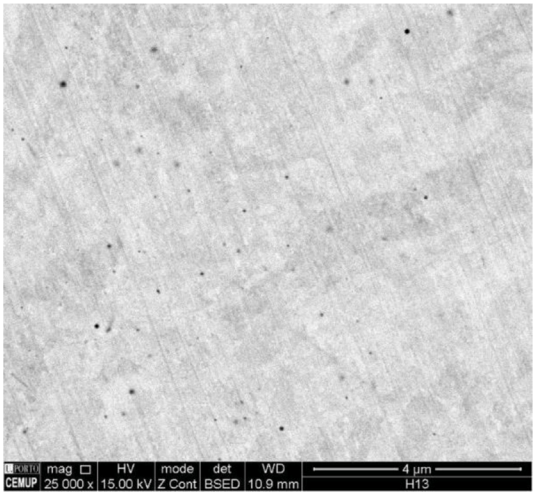

Fig. 13 – Micrography (SEM) of AISI H13 as-built after PBF/SLM processing, XY plan.

Table 3 – Microhardness of AISI H13 with and without the addition of V and C.

	Microhardness (HV)	Microhardness (GPa)
AISI H13 (quenching and tempering)[a]	556	5.56
PBF/SLM AISI H13	564 ± 21	5.64 ± 0.21
PBF/SLM H13+5V (wt%)	339 ± 16	3.39 ± 0.16
PBF/SLM H13+5V + 0.8C (wt%)	671 ± 23	6.71 ± 0.23

[a] ASM vol. 1 Handbook; Properties and Selection: Irons Steels and High-Performance Alloys, ASM, 1991, pp.1797, 1822.

-Electron Backscatter Diffraction) (Fig. 13) is visible some black points which are identified by EDS as vanadium compounds. The possibility of having vanadium carbides located along the grain boundaries does not agree with the grain size observed, due to the dimensional anisotropy created by the PBF/SLM cooling rate.

The microhardness of the PBF/SLM 3D top specimen is similar to the quenched microstructure of conventional bulk AISI H13 (Table 3). In conventional alloy steels, vanadium is an element with a high aptitude to react with carbon, with a high ability during cooling to form vanadium carbides, depending on its content and carbon percentage of steel [29]. This means transforming the steel into a composite, where the reinforcement dimensions (carbide) depend on the cooling rate. The effect of the increase of vanadium content in AISI H13 will be analyzed in the following items.

3.1. *Effect of vanadium addition in the microstructure of AISI H13 after PBF/SLM*

As referred, the material analyzed was close to the surface (last melting layers) in order to avoid other post heat treatments (tempering) during the building of the 3D object. Besides, the thermal conductivity of H13, along with the non-heating of the bed powder, does not contribute to carbide growth.

The X-ray diffractogram of the PBF/SLM 3D object (top) (Fig. 14) does not show diffraction peaks of austenite and vanadium, present in the feedstock, and neither of V_xC_y carbides.

However, the optical micrography (Fig. 15a) shows a significant improvement of vanadium carbides inside of the matrix and in grain boundaries, but without a significant decrease in grain size. The SEM images (Fig. 15b and c and 16) validate the presence of nanocarbides of vanadium inside and along the grain boundaries.

The significant decrease in the hardness (Table 3) can be attributed to the vanadium excess. Carbon is needed to harden the matrix, and due to the addition of vanadium, it attains values close to 0%. The 5.97 at. % (6 wt %) of vanadium (1% from AISI H13 powder and 5% from V powder added) and considering V partition coefficient, makes 4.78 (at. %) responsible for forming V_xC_y. Moreover, the relationship C/V is previewed in V_xC_y (1–0.5) as maximum and minimum carbon available from 1.52 to 2.72 at.%. However, the maximum carbon in the steel is 1.64 at. %, which means after the formation V_xC_y, there is not enough carbon in the matrix able to contribute to hardening the matrix (martensite).

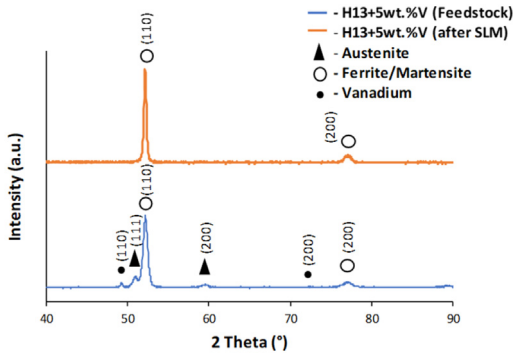

Fig. 14 – X-ray diffractograms of H13+5V (wt.%) as-built by PBF/SLM (top) and feedstock (bottom).

The vanadium nanocarbide was analyzed by Transmission Electron Microscopy (TEM), as depicted in Fig. 16. In Fig. 17a, the high-resolution image showcases the microscopic morphology and Fig. 17b displays the respective selected area electron diffraction (SAED) pattern.

The diffraction spots of the SAED pattern with significant intensity correspond to VxCy, exhibiting a face-centered cubic (fcc) crystal structure with lattice parameter of a = 0.416 nm (Crystallographic structure of vanadium carbide precipitates in a model Fe–C–V steel, Thierry Epicier). Commonly, all octahedral gaps are occupied with carbon atoms. However, the SAED pattern confirms that these interstitial vacancies are also occupied by V_6C_5, which possesses a simple hexagonal superlattice (HCP) characterized by lattice parameters [30] a' = 0.509 nm and c' = 1.440 nm. During cooling, VxCy undergoes a transformation into the stable V6C5 structure due to the presence of carbon vacancies. However, this transformation remains incomplete under non-equilibrium conditions, during SLM processing [31].

The increase of the mechanical properties obliges to a concomitant addition of an allotrope of carbon to maintain the steel carbon (matrix) and the excess of carbon to be used to produce the maximum of V_xC_y.

3.2. *Effect of carbon addition in the microstructure of H13+5V (wt.%) after PBF/SLM*

The total effect of vanadium in the PBF/SLM microstructures based on H13 obliges the addition of 0.8 wt% of carbon, corresponding in the feedstock to 5.09 at. %C.

Although the X-ray diffractogram of the PBF/SLM 3D object (top) (Fig. 18) does not exhibit diffraction peaks associated with the austenite and vanadium present in the initial

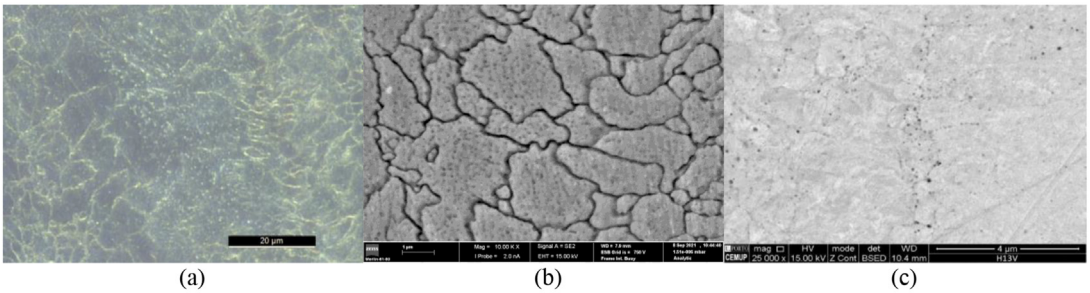

Fig. 15 – Optical microscopic image (OM) of AISI H13+5V (wt.%) as-built, in the XY plane (400x) (left), and a detail (SEM) (right).

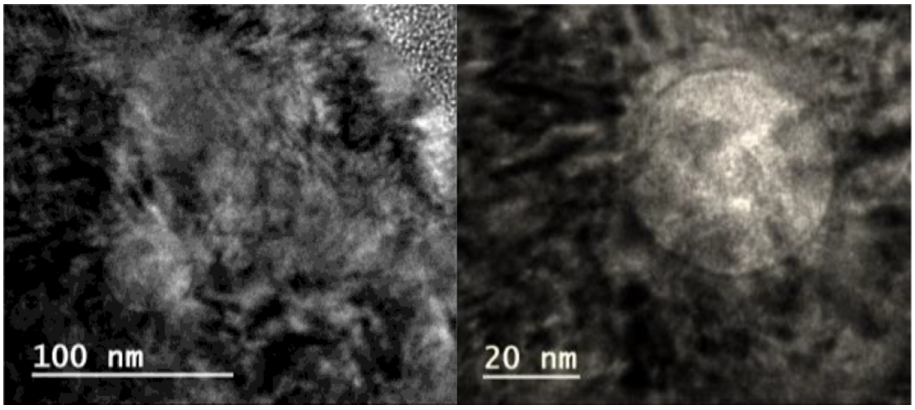

Fig. 16 – TEM image of M_xC_y present in thin foils extracted by FIB of H13+5V wt.%.

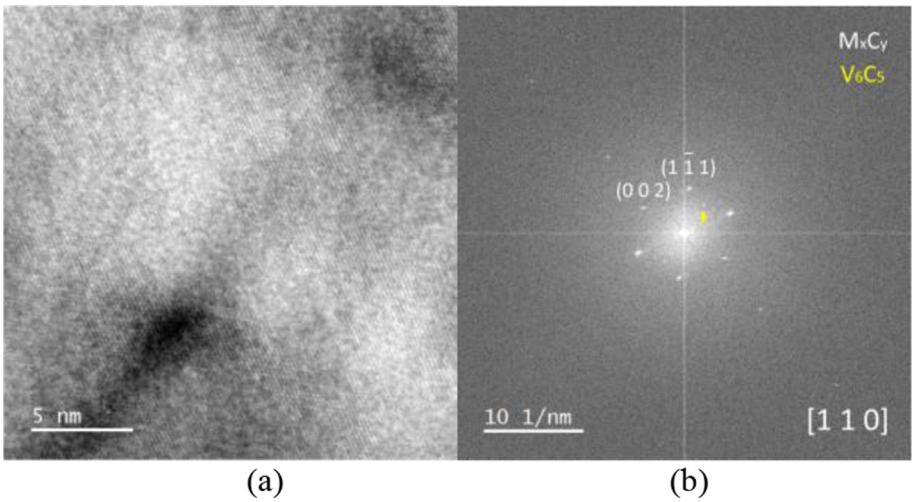

Fig. 17 – HRTEM analysis of M_xC_y and V_6C_5 phases present in thin foils extracted by FIB of H13+5V wt.% in the XY plane, after PBF/SLM processing (a), and respective SAED pattern (b).

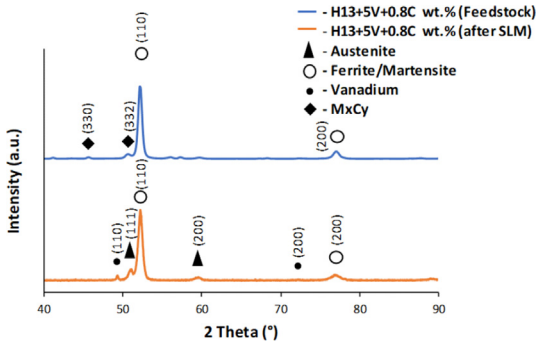

Fig. 18 – X-ray diffractograms of H13+5V+0.8C (wt.%) as-built by PBF/SLM (top) and feedstock (bottom).

feedstock, it does reveal low intensity peaks of VxCy carbides, in accordance to file 00-019-1394 of the international center for diffraction data JCPDS-ICDD 2000.

The effect of the vanadium carbides in the steel matrix has a significant role in the homogenization of grain size dimensions (Fig. 19). An anisotropic structure (Fig. 20 left) is substituted by equiaxial grains (Fig. 20, right).

The V_xC_y after PBF/SLM processing (Figs. 19 and 20) must be substituted by (V, Mo) $_xC_y$ (Fig. 21), which means the carbide should be represented by M_xC_y with M = V, Mo as in bulk alloy steels.

The presence in the last layers formed by PBF/SLM of M_xC_y means that these carbides are not the result of tempering. They are primary nanocarbides, and this is disaccording to the referred authors [15–18] that affirmed that there are no carbides after PBF/SLM.

Without modifying the carbon content of conventional bulk quenched AISI H13 steel, the effect of the nano M_xC_y increasing contributes to the decrease of about 40% in microhardness (Table 3).

The values of hardness were also assessed through nanoindentation tests and reduced Young modulus calculated (Table 4). Due to the non-linear relationship between hardness and the square root of the applied load, which results in a faster increase in hardness for lighter loads, the surface hardness values may be higher compared to microhardness. This effect becomes noticeable when the applied load during surface hardness testing is relatively modest, in contrast to the load used in microhardness testing, according to Meyer's Law. As anticipated, the nanocarbides content of H13+5V+G contributed to the highest hardness, superior to the

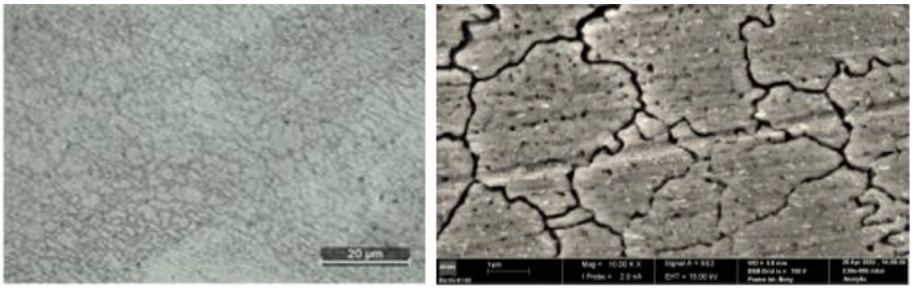

Fig. 19 – Optical microscopic image (OM) of H13+5V+0.8C (wt.%) as-built, in the XY plane (400x) (left), and a detail (SEM) (right).

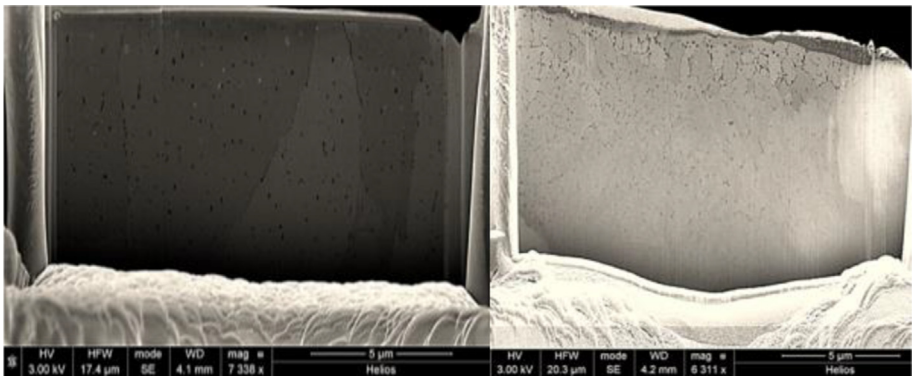

Fig. 20 – SEM microstructures of thin foils extracted by FIB of H13 + 5%V(left) and H13+5 V+0.8 C wt.% (right) in the XY plane after PBF/SLM processing.

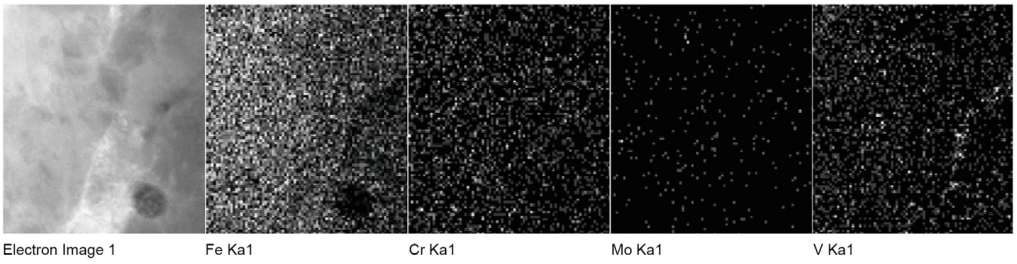

Fig. 21 – Scanning Transmission Electron Microscopy (STEM) image of H13+5V+0.8 C wt.% and respective Electron Energy Loss Spectroscopy (EELS) mapping of Fe, Cr, V, and Mo in H13+5V+0.8 C wt.%.

Table 4 – Nanoindentation of AISI H13 with and without the addition of V and C after PBF/SLM.

Specimen Ref.	Maximum Indentation Load (mN)	Hardness (GPa)	Reduced Young Modulus (GPa)
H13	1.5	9.2 ± 0.8	209 ± 18
H13+5V	1.5	7.2 ± 1.4	219 ± 28
H13+5V+0.8C	1.5	15.9 ± 3.1	351 ± 34

Table 5 – Nanohardness and microhardness of high-speed steels AISI M42 and AISI H13.

	Maximum Indentation Load (mN)	Nanohardness (GPa)	Macrohardness (HV)
AISI M42 [33] bulk	10	6.79 ± 0.51	1050
AISI H13 [32] powder (quenching and tempering)	30	8.1	660

conventional high-speed steel (Table 5). However, H13+5V presents a lower hardness value compatible with a bainitic microstructure of AISI H13. After PBF/SLM, the vanadium addition to the AISI H13 powders contributed, to the increase of hardening precipitates content, while combining with the carbon of the steel matrix, leading to a significant hardness decreasing of the matrix, similar to a low carbon steel.

4. Conclusions

The role of vanadium content in H13 in processing steel powder by PBF/SLM as a new route to build H13 tool steel 3D objects. It can induce superior surface properties, depending on the vanadium content related to the carbon necessary to improve vanadium carbide content without modifying the characteristics of a conventional H13 heat-treated (quenching and tempering). This contributes to avoiding the need for hard coatings, decreasing adhesion problems and costs. Furthermore, it was demonstrated that the presence of vanadium nanocarbides after PBF/SLM cooling is a reality, which also promotes grain size control and, consequently, mechanical properties. Future research work should contribute to the vanadium content limits on the PBF/SLM surface (XY) of 3D objects and establishment of the compositional gradient function of the 3D object geometry.

Declaration of competing interest

The authors declare that they have no known competing financial interests or personal relationships that could have appeared to influence the work reported in this paper.

Acknowledgments

This research is sponsored by national funds through FCT – Fundação para a Ciência e a Tecnologia, under the project UIDB/00285/2020 and LA/P/0112/2020, and the project POCI-01-0247-FEDER-047156 funded by FEDER funds through COMPETE2020.

REFERENCES

[1] Ngo TD, Kashani A, Imbalzano G, Nguyen KTQ, Hui D. Additive manufacturing (3D printing): a review of materials, methods, applications and challenges. Compos B Eng 2018;143:172–96. https://doi.org/10.1016/j.compositesb.2018.02.012.

[2] Mehrpouya M, Dehghanghadikolaei A, Fotovvati B, Vosooghnia A, Emamian SS, Gisario A. The potential of additive manufacturing in the Smart factory industrial 4.0: a review. Appl Sci 2019;9(18). https://doi.org/10.3390/app9183865.

[3] Mazur M, Leary M, McMillan M, Elambasseril J, Brandt M. SLM additive manufacture of H13 tool steel with conformal cooling and structural lattices. Rapid Prototyp J 2016;22(3):504–18. https://doi.org/10.1108/RPJ-06-2014-0075.

[4] Mazur M, Brincat P, Leary M, Brandt M. Numerical and experimental evaluation of a conformally cooled H13 steel injection mould manufactured with selective laser melting. Int J Adv Manuf Technol 2017;93(1):881–900. https://doi.org/10.1007/s00170-017-0426-7.

[5] Santhoshsarang DM, Divya K, Telasang G, Soundarapandian S, Bathe R, Padmanabham G. Additively manufactured high-performance conformally cooled H13 tool steel die insert for pressure die casting. Trans Indian Natl Acad Eng 2021;6(4):1037–48. https://doi.org/10.1007/s41403-021-00233-y.

[6] Clemente MR, Oliveira Panão MR. Introducing flow architecture in the design and optimization of mold inserts cooling systems. Int J Therm Sci 2018;127:288–93. https://doi.org/10.1016/j.ijthermalsci.2018.01.035.

[7] Sabau AS, Bejan A, Brownell D, Gluesenkamp K, Murphy B, List F, Carver K, Schaich CR, Klett JW. Design, additive manufacturing, and performance of heat exchanger with a novel flow-path architecture. Appl Therm Eng 2020;180:115775. https://doi.org/10.1016/j.applthermaleng.2020.115775.

[8] Dzukey GA, Yang K, Wang Q, Zhuang B, Hou W. Porosity, hardness, friction and wear performance analysis of H13 SLM-formed samples. J Mater Eng Perform 2020;29(8):4957–66. https://doi.org/10.1007/s11665-020-04999-0.

[9] Kumar S, Maity SR, Patnaik L. Mechanical and scratch behaviour of TiAlN coated and 3D printed H13 tool steel. Adv Mater Process Technol 2021;0(0):1–15. https://doi.org/10.1080/2374068X.2021.1927642.

[10] Quinlan HE, Hasan T, Jaddou J, Hart AJ. Industrial and consumer uses of additive manufacturing: a discussion of capabilities, trajectories, and challenges. J Ind Ecol 2017;21(S1):S15–20. https://doi.org/10.1111/jiec.12609.

[11] Bhuvanesh Kumar M, Sathiya P. Methods and materials for additive manufacturing: a critical review on advancements and challenges. Thin-Walled Struct 2021;159:107228. https://doi.org/10.1016/j.tws.2020.107228.

[12] Wang M, Wu Y, Wei Q, Shi Y. Thermal fatigue properties of H13 hot-work tool steels processed by selective laser melting. Metals 2020;10(1):116. https://doi.org/10.3390/met10010116.

[13] Vukkum VB, Christudasjustus J, Darwish AA, Storck SM, Gupta RK. Enhanced corrosion resistance of additively manufactured stainless steel by modification of feedstock. npj Mater Degrad 2022;6(1):2. https://doi.org/10.1038/s41529-021-00215-z.

[14] Wu L, Das S, Gridin W, Leuders S, Kahlert M, Vollmer M, Niendorf T. Hot work tool steel processed by laser powder bed fusion: a review on most relevant influencing factors. Adv Eng Mater 2021;23(7):2100049. https://doi.org/10.1002/adem.202100049.

[15] Fonseca EB, Gabriel AHG, Araújo LC, Santos PLL, Campo KN, Lopes ESN. Assessment of laser power and scan speed influence on microstructural features and consolidation of AISI H13 tool steel processed by additive manufacturing. Addit Manuf 2020;34:101250. https://doi.org/10.1016/j.addma.2020.101250.

[16] Yonehara M, Ikeshoji T-T, Nagahama T, Mizoguchi T, Tano M, Yoshimi T, Kyogoku H. Parameter optimization of the high-power laser powder bed fusion process for H13 tool steel. Int J Adv Manuf Technol 2020;110(1):427–37. https://doi.org/10.1007/s00170-020-05879-6.

[17] Krell J, Röttger A, Geenen K, Theisen W. General investigations on processing tool steel X40CrMoV5-1 with selective laser melting. J Mater Process Technol 2018;255:679–88. https://doi.org/10.1016/j.jmatprotec.2018.01.012.

[18] Lee J, Choe J, Park J, Yu J-H, Kim S, Jung ID, Sung H. Microstructural effects on the tensile and fracture behavior of selective laser melted H13 tool steel under varying conditions. Mater Char 2019;155:109817. https://doi.org/10.1016/j.matchar.2019.109817.

[19] Deirmina F, Peghini N, AlMangour B, Grzesiak D, Pellizzari M. Heat treatment and properties of a hot work tool steel fabricated by additive manufacturing. Mater Sci Eng, A 2019;753:109–21. https://doi.org/10.1016/j.msea.2019.03.027.

[20] Katancik M, Mirzababaei S, Ghayoor M, Pasebani S. Selective laser melting and tempering of H13 tool steel for rapid tooling applications. J Alloys Compd 2020;849:156319. https://doi.org/10.1016/j.jallcom.2020.156319.

[21] AlMangour B, Grzesiak D, Yang J-M. Nanocrystalline TiC-reinforced H13 steel matrix nanocomposites fabricated by selective laser melting. Mater Des 2016;96:150–61. https://doi.org/10.1016/j.matdes.2016.02.022.

[22] Ren B, Lu D, Zhou R, Li Z, Guan J. Preparation and mechanical properties of selective laser melted H13 steel. J Mater Res 2019;34(8):1415–25. https://doi.org/10.1557/jmr.2019.10.

[23] Narvan M, Al-Rubaie KS, Elbestawi M. Process-structure-property relationships of AISI H13 tool steel processed with selective laser melting. Materials 2019;12(14):2284. https://doi.org/10.3390/ma12142284.

[24] Oliver WC, Pharr GM. An improved technique for determining hardness and elastic modulus using load and displacement sensing indentation experiments. J Mater Res 1992;7(6):1564–83. https://doi.org/10.1557/JMR.1992.1564.

[25] Guanghua Y, Xinmin H, Yanqing W, Xingguo Q, Ming Y, Zuoming C, Kang J. Effects of heat treatment on mechanical properties of H13 steel. Met Sci Heat Treat 2010;52(7):393–5. https://doi.org/10.1007/s11041-010-9288-4.

[26] Baker TN. Processes, microstructure and properties of vanadium microalloyed steels. Mater Sci Technol 2009;25(9):1083–107. https://doi.org/10.1179/174328409X453253.
[27] Xing W, Meng F, Yu R. A new type of vanadium carbide V5C3 and its hardening by tuning fermi energy. Sci Rep 2016;6(1):21794. https://doi.org/10.1038/srep21794.
[28] Wang G, Ouyang H, Fan C, Guo Q, Li Z, Yan W, Li Z. The origin of high-density dislocations in additively manufactured metals. Mater Res Lett 2020;8(8):283–90. https://doi.org/10.1080/21663831.2020.1751739.
[29] Billingham J, Bell PS, Lewis MH. Vacancy short-range order in substoichiometric transition metal carbides and nitrides with the NaCl structure. I. Electron diffraction studies of short-range ordered compounds. Acta Crystallogr A 1972;28(6):602–6. https://doi.org/10.1107/S0567739472001524.
[30] Liujie X, Shizhong W, Jiandong X, Yan L, Rui L. Phase structure and fine microstructure of in-situ vanadium carbides in cast high-vanadium high-speed steel. Met Mater Int 2006;12(5):371–5. https://doi.org/10.1007/BF03027702.
[31] Lai S, Gan M, Xu L, Tan Z, Li Z, Wei S, Jiang Y, Feng J, Chong X. Stability and fracture mechanism of α-Fe/V6C5 interface in high vanadium Fe-based alloys by first-principles calculations. Surface Interfac 2023;36:102573. https://doi.org/10.1016/j.surfin.2022.102573.
[32] Poirier D, Thomas Y, Guerreiro B, Martin M, Aghasibeig M, Irissou E. Improvement of tool steel powder cold sprayability via softening and agglomeration heat treatments. J Therm Spray Technol 2022;31(1):145–58. https://doi.org/10.1007/s11666-022-01320-4.
[33] Liu Y, Li D, Shao Q, Ma H, Kang J, Su R. Study on friction and wear behaviors of M42 high speed steel. J Phys Conf 2022;2168(1):012025. https://doi.org/10.1088/1742-6596/2168/1/012025.